ACCEPTED VERSION

Timothy C.W. Lau, Graham J. Nathan

A method for identifying and characterising particle clusters in a two-phase turbulent jet

Final publication at http://dx.doi.org/10.1016/j.ijmultiphaseflow.2016.10.002

PERMISSIONS

https://www.elsevier.com/about/our-business/policies/sharing

Accepted Manuscript

Authors can share their accepted manuscript:

[…]

After the embargo period

- via non-commercial hosting platforms such as their institutional repository
- via commercial sites with which Elsevier has an agreement

In all cases accepted manuscripts should:

- link to the formal publication via its DOI
- bear a CC-BY-NC-ND license – this is easy to do, click here to find out how
- if aggregated with other manuscripts, for example in a repository or other site, be shared in alignment with our hosting policy
- not be added to or enhanced in any way to appear more like, or to substitute for, the published journal article

Embargo

1879-3533	International Journal of Multiphase Flow	24 months

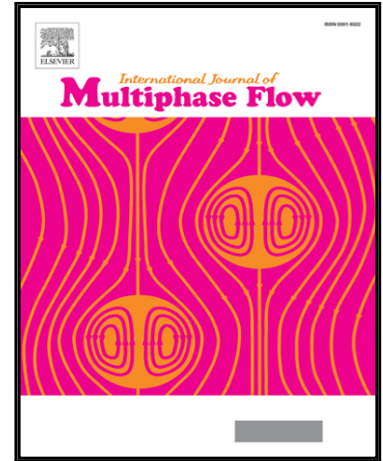**30 January 2019**

---

http://hdl.handle.net/2440/105269

Accepted Manuscript

A method for identifying and characterising particle clusters in a two-phase turbulent jet

Timothy C.W. Lau, Graham J. Nathan

Highlights

- Developed a method to identify and characterise particle clusters in a turbulent jet

- Clusters observed at exit plane, suggesting they are generated inside the pipe

- Clusters tended to form filament-like structures of high aspect ratio

- Evidence that the preferred clustering length scale is 0.17D

A method for identifying and characterising particle clusters in a two-phase turbulent jet

Timothy C. W. Lau[1],[*], Graham J. Nathan

Centre For Energy Technology, School of Mechanical Engineering
The University of Adelaide, 5005 SA, Australia

Abstract

A novel technique for identifying and characterising clusters of particles from measurements within a densely seeded two-phase flow is reported. This technique involves the smoothing of normalised instantaneous planar images of particle concentration followed by the application of a robust and unambiguous dynamic threshold to identify particle clusters. Also reported is a method to extract quantitative cluster data including cluster length, width and number of branches. The method employs an algorithm to morphologically skeletonize images of clusters, and subsequently, prune skeleton branches to select those which most strongly represent the shape of the cluster. Together, these techniques have been shown to identify and characterise two-dimensional slices of three-dimensional particle clusters of complex shapes, including those that are bent, wrinkled and branched, with an uncertainty of $\approx 4\%$ relative to the manually determined values.

This method was applied to planar measurements of particles in a heavily seeded turbulent jet with an exit Stokes number of $Sk_D = 1.4$ and Reynolds number of $Re_D = 10,000$, based on the pipe diameter, D. The results show that particle clusters are already present at the exit plane and have a characteristic width that is narrowly distributed around an average value of $\approx 0.17D$. This implies that particle clusters are generated inside the pipe at this preferred length scale. The results also show that the average cluster length at the pipe exit is $\approx 1.0D$, which, together with the observation that the clusters are oriented at oblique angles to the axis of the jet, suggests that the length of these clusters within the pipe is limited by the pipe diameter. The aspect ratio of the cluster slices was found to be typically $AR \approx 6 - 7$, consistent with the observations that the clusters form long, thin, filament-like structures.

Keywords: particle clusters, preferential concentration, skeletonization

1. Introduction

Particle-laden turbulent jets are utilised in many scientific and industrial applications, most notably in the applications for the combustion of pulverised fuels, the processing of minerals, and more recently, in concentrating solar thermal reactors. In these flows, it has been observed that the instantaneous spatial distribution of particles differs significantly from a random distribution, with particles within the flow being preferentially distributed into instantaneous regions of localised, high particle concentration called "clusters" (Birzer et al., 2011a,b; Longmire and Eaton, 1992; Zimmer and Ikeda, 2003). This naturally occurring phenomenon has been shown to have a significant impact on reacting flows, affecting heat transfer, ignition distance, ignition temperature, stoichiometry and emissions, because they imply a non-uniform distribution of fuel within the flame (Abbas et al., 1993; Anna-

malai and Ryan, 1992; Cassel and Liebman, 1959; Smith et al., 2002). However, while their significance is well understood, a quantitative analysis of the significance of particle clustering in two-phase flows is currently limited. In particular, a systematic and statistical assessment of particle clustering in turbulent flows in the two-way coupling regime, whereby the particle number density is sufficiently high that the particles affect the gas-phase, is almost entirely absent. Therefore, the overall aim of the present paper is to begin to meet this need for quantitative measurements of clusters in flows with high particle number density.

Previous studies on preferential concentration of particles have highlighted the importance of the Stokes number in determining the extent of particle clustering (Aliseda et al., 2002; Bec et al., 2007; Calzavarini et al., 2008; Eaton and Fessler, 1994; Fessler et al., 1994; Gualtieri et al., 2009; Hogan and Cuzzi, 2001; Monchaux et al., 2010; Rouson and Eaton, 2001; Wang and Maxey, 1993; Yoshimoto and Goto, 2007), where the Stokes number is defined as the ratio of time-scales of particle response to characteristic fluid eddy. In particular, clustering has been shown to

---

[*]Corresponding author
Email addresses: `timothy.lau@adelaide.edu.au` (Timothy C. W. Lau), `graham.nathan@adelaide.edu.au` (Graham J. Nathan)
[1]Tel:+61 8 83183960

be most significant where the Stokes number is of order unity (Bec et al., 2007; Calzavarini et al., 2008; Fessler et al., 1994; Gualtieri et al., 2009; Rouson and Eaton, 2001; Wang and Maxey, 1993; Yoshimoto and Goto, 2007). Because turbulence comprises a spectrum of scales, from the smallest dissipative length scales to the largest inertial length scales, it is likely that more than one length scale can influence particle clustering (Aliseda et al., 2002; Bec et al., 2007; Eaton and Fessler, 1994; Goto and Vassilicos, 2006; Gualtieri et al., 2009; Monchaux et al., 2010; Yoshimoto and Goto, 2007). Evidence for this can be found in the range of length scales associated with clusters, such as their length, width and spacing. Hence there is a need for detailed measurements of cluster dimensions and shapes.

Despite their importance, there is a lack of data of the magnitude of cluster length scales, in part because of the limitations of current methods to determine them. While methods of analyzing particle clustering, such as statistical box counting (Aliseda et al., 2002; Bec et al., 2007; Fessler et al., 1994; Hogan and Cuzzi, 2001; Rouson and Eaton, 2001; Wang and Maxey, 1993), the radial distribution function (Gualtieri et al., 2009; Salazar et al., 2008), the pair correlation function (Goto and Vassilicos, 2006; Saw et al., 2008; Yoshimoto and Goto, 2007), Minkowski functionals (Calzavarini et al., 2008) and Voronoï analysis (Monchaux et al., 2010; Obligado et al., 2014) are capable of providing useful information such as the characteristic cluster length scale and the degree of global clustering, they crucially require that individual particles be spatially resolved. This, in turn, requires probe sizes that are significantly smaller than the inter-particle spacing. As the limiting probe dimension in typical laser diagnostic measurements is the light sheet thickness, the resolution of individual particles is only possible at low volumetric loadings. This limits the detection of clusters with existing methods to the dilute regime, i.e., to flow conditions whereby the particle volume loading, β, and/or the particle number density, $\tilde{N}_p$, is small (see table 1). As there is significant practical and scientific interest in two-phase flows in the two-way and four-way coupling regimes, where volumetric loadings are large (Elghobashi, 2006), there is a clear need for a method to detect clusters from images in which individual particles are not resolved. Furthermore, the requirement to capture the largest length scales of a cluster, which can be of the order of the local jet diameter (Birzer et al., 2011a,b), together with the practical constraints of detector arrays also limit the capacity to resolve both the particle size and the maximum dimensions of a cluster. This provides a further need for methods to detect clusters under conditions in which individual particles are not resolved.

The identification and characterisation of particle clusters in a densely-seeded turbulent flow from planar images is non-trivial, because particle clusters within the same flow may have different sizes, concentrations, orientations and shapes. In previous studies this process typically involves the use of an arbitrary global threshold in conjunction with spatially averaging or binning of the particle concentration field across a specified length scale (Birzer et al., 2011a,b; Monchaux et al., 2012; Zimmer and Ikeda, 2003). While no absolute measure of a cluster is possible, it is desirable to replace the use of these arbitrary parameters with statistically robust parameters that are unambiguous and justifiable.

Once clusters are identified, a further step is required to measure and classify the characteristic dimensions of these clusters. One such scheme, albeit for a different class of flow, was introduced by Qamar et al. (2011), who fitted equivalent ellipses to soot sheets to determine their characteristic lengths and widths. This method was further improved by Chan et al. (2014), who modified the equivalent-ellipse method for use with curved or bent soot sheets. However, as is demonstrated within the analysis in the current paper, neither of these methods are suitable for use on clusters with highly irregular, wrinkled, or branched shapes.

Therefore, the aim of the present study is to develop a method for the automated identification and characterisation of two-dimensional slices through three-dimensional particle clusters, obtained from planar images, with variable and complex shapes such as occur in turbulent, densely-seeded, two-phase flows. This method should be robust, i.e., it should be insensitive to the variability in absolute particle concentration, cluster shape and cluster size. This paper further aims to demonstrate its capacity to provide quantitative, statistical information on cluster dimensions and distributions, paving the way for an improved understanding of the phenomenon of particle clustering and instantaneous preferential concentration in two-phase turbulent flows.

It should be noted that the identification of two dimensions of a slice through a cluster from a planar image can be readily extended to a three-dimensional measurement by the application of volume rendering from multiple parallel sheets. Analogous methods to obtain volumetric data from parallel images have been performed in both non-reacting (Cheng et al., 2011; Thurow and Lynch, 2009; Wellander et al., 2011) and reacting (Cho et al., 2014; Gamba et al., 2013) conditions. In addition, two-dimensional data are already useful, with much important understanding already obtained from such images (Birzer, 2012; Birzer et al., 2011a,b; Chan et al., 2014; Fessler et al., 1994; Longmire and Eaton, 1992; Monchaux et al., 2010; Smith et al., 2002; Qamar et al., 2011; Zimmer and Ikeda, 2003). For these reasons, the present method is developed and demonstrated using a single planar light sheet.

2. Experimental arrangement

The experiment consisted of a particle-laden turbulent jet of air issuing from a long, round pipe into a low-velocity co-flow, as shown in figure 1. The pipe was mounted vertically downward within a wind tunnel to avoid gravity bias. The diameter of the pipe was $D = 12.7$mm while the length

First author	d_p (μm)	ρ_p(kg/m^3)	β	$\tilde{N}_p$	LST (μm)	Θ_b (mm^{-3})	Δ_p (μm)	$\tilde{P}_{>1}$ (%)
Aliseda (2002)	≈ 25	1000	1.5×10^{-5} to 7.5×10^{-5}	O(10^{-3}) to O(10^{-2})	≈ 1000	≈ 2 to 10^*	≈ 478 to 817^*	≈ 0.1 to 1.1^*
Fessler (1994)	25 to 90	700 to 8800	O(10^{-5}) to O(10^{-4})*	N/A	≈ 1000	≈ 3	≈ 607 to 1257^*	N/A
Monchaux (2010)	≈ 50 to 100	1000	O(10^{-6}) to O(10^{-5})	O(10^{-4}) to O(10^{-3})*	≈ 2000	≈ 0.03 to 0.5^*	≈ 1300 to 3200^*	O(10^{-2})to O(10^{-1})*
Obligado (2014)	≈ 50	1000	O(10^{-5}) to O(10^{-4})	O(10^{-3}) to O(10^{-2})	≈ 1000	≈ 0.8 to 3^*	≈ 690 to 1094^*	≈ 0.3 to 1.4^*
Salazar (2008)	≈ 6.1	1375	O(10^{-7})	N/A	N/A	≈ 2	$\approx 1000^*$	N/A
Current	20	1200	4×10^{-4}	≈ 0.1	≈ 350	≈ 100	≈ 220	≈ 4.1 to 8.3

Table 1: Summary of conditions utilised in previous experimental measurements of particle clustering. Also included are the conditions for the current experiment. Here d_p is the particle diameter, ρ_p is the particle material density, β is the volume loading, $\tilde{N}_p$ is the number of particles per pixel (bulk), LST is the light sheet thickness, Θ_b is the bulk particle number density, Δ_p is the average inter-particle spacing and $\tilde{P}_{>1}$ is the relative probability that 2 or more particles are located within the same measurement volume. Values denoted by the asterisk are values that have been inferred from published data.
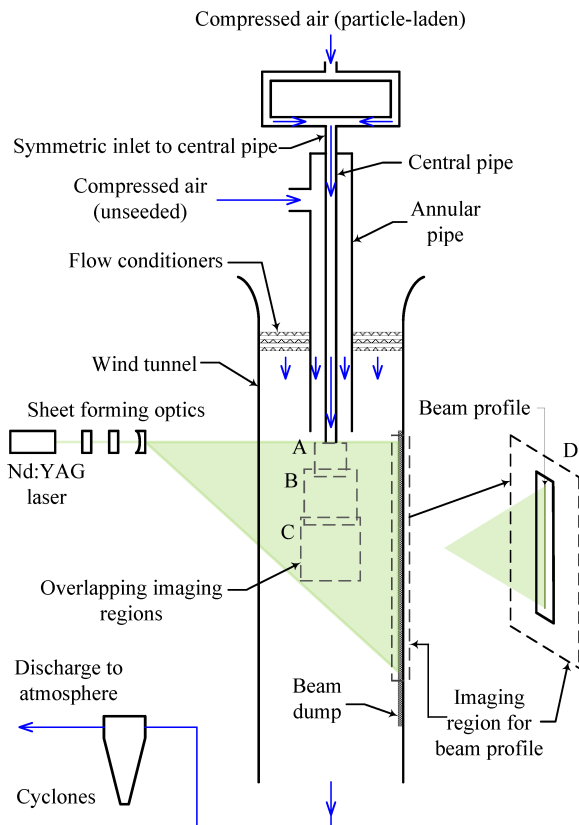

Figure 1: Schematic diagram of experimental arrangement.

of the pipe was $L_p = 2080$mm, leading to a pipe length-to-diameter ratio of $L_p/D \approx 164$. This ratio was previously found to be sufficient to closely approach fully-developed two-phase flow at the pipe exit (Lau and Nathan, 2014). The jet bulk velocity was fixed at $U_b = 12$m/s, resulting in an exit Reynolds number of $Re_D = 10,000$, while the co-flow velocity was fixed at 1m/s, resulting in a sufficiently high jet-to-co-flow velocity ratio such that the near field of the jet approximates a free jet (Antonia and Bilger, 1976).

The particles were spherical with a diameter of $d_p = 20 \pm 1\mu$m, resulting in a mono-disperse two-phase jet. The particles were made of a polymer with a density of $\rho_p = 1200$kg/m^3, resulting in an exit Stokes number of

$$Sk_D = \frac{\rho_p d_p^2 U_b}{18\mu D} = 1.4, \tag{1}$$

where μ is the dynamic viscosity of the working fluid. The particle mass loading, defined as the ratio of the particle phase mass flow rate to the gas phase mass flow rate, was fixed at $\phi = 0.4$. This is sufficiently high to result in significant interactions between the gas and particle phases, that is, the flow was in the two-way coupling regime (El-ghobashi, 2006).

Planar measurements of particle concentration (number density), $\Theta(x,r)$, where x and r are the axial and radial directions, respectively, was measured using planar nephelometry, which infers particle number density from the intensity of the Mie scattering from the particles. In the current experiments where a mono-disperse particle size distribution is utilised, this method provides instantaneous planar snapshots of particle concentration throughout the region of interest. Additionally, this method does not necessarily require the identification of individual particles and therefore has the benefit that it can be applied to densely seeded flows and large measurement regions (Birzer et al., 2011a). The source of illumination

4

was a frequency-doubled (532nm), Nd:YAG laser, with a fixed pulsing frequency of 10Hz and a laser power of approximately 150mJ per pulse. A laser sheet of thickness $\approx 350 \pm 50\mu$m was generated from the beam which was used to illuminate the entire measurement region. Three Kodak Megaplus cameras were used to measure the profile and intensity of the transmitted sheet, from very close to the exit plane ($x/D \approx 0.01$) to an axial distance of $x/D = 30$, while a fourth Kodak Megaplus camera was used to measure the beam profile at the down-beam side of the jet (see figure 1). This latter measurement allowed the intensity of the images to be corrected for variation in beam profile and optical attenuation on a shot-by-shot basis (Cheong et al., 2015; Kalt and Nathan, 2007). The attenuation correction algorithm was capable of performing corrections on a per-pixel basis because the properties of the particles remained constant and mono-disperse particles were used in the experiment. The images obtained from the three cameras were combined together to form a single array of particle concentrations for set of instantaneous images during post-processing. The proportion of pixels that were saturated (relative to the total number of pixels) was less than 8×10^{-4}.

The settings for the three cameras used to record the particle distributions are presented in table 2. As can be seen the average particle spacing, Δ_p was typically smaller than the largest probe dimension (here the light sheet thickness). Also presented is the average number of particles per pixel, $\tilde{N}_p$, as well as the probability that a pixel records more than 1 particle (normalised to the probability that a pixel records *any* number of particles), $\tilde{P}_{>1}$. Although the average number of particles per pixel was typically less than unity, a minimum of 4% of all data involve the measurement of multiple particles per pixel. This can be considered a lower bound, as the calculated value of $P_{>1}$ assumes that the particles are randomly distributed (i.e., no clustering process exists) and have image sizes that are equal to or smaller than 1 pixel. Additionally, the instantaneous values of particle number density within the current flow was found to be significantly higher than the mean (time-average), which further increases the probability of measuring multiple particles per pixel. To illustrate this, the maximum particle concentration, Θ_{max}, was calculated by taking the 95th percentile of the ensemble of instantaneous concentration values. The measured maximum concentration, normalised by the bulk concentration, Θ_b, along the jet centreline is presented in figure 2. The results show that the peak concentration may exceed the bulk concentration by a factor of 10 or more. This results in a minimum inter-particle spacing of $\Delta_{p,min} \approx 100\mu$m, which is significantly smaller than the laser sheet thickness ($\approx 350\mu$m). Furthermore, a peak value of $\Theta_{max}/\Theta_b \gtrsim 10$ also results in the peak number of particles per pixel to exceed unity and leads to a value of $\tilde{P}_{>1} \approx 41\%$. Therefore, in the current experiments, the imaging of multiple particles per pixel, and/or overlapping particles, is expected to occur regularly. This re-iterates the need for a cluster mea-
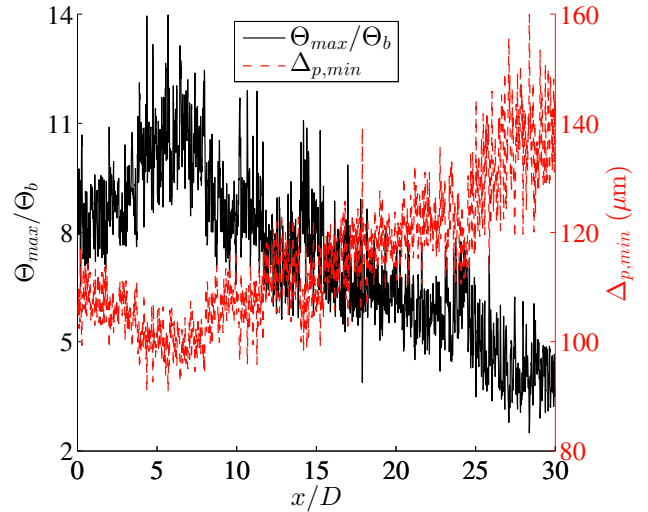

Figure 2: The measured maximum particle concentration (95th percentile), Θ_{max}, normalised by the bulk concentration, Θ_b, along the centreline of the jet. Also included is the minimum inter-particle spacing, $\Delta_{p,min}$, which was calculated from the particle concentration data.

surement method which does not rely on the identification of individual particles.

The true axis of the jet was determined by fitting a Gaussian curve to the intensity distribution of the mean (time-averaged) image at each axial location, and then connecting the location of the peaks of the fitted curves using a straight line. This axis was found to be parallel to the centreline of the image to within $\pm 0.2°$. Additionally, the symmetry of the jet was confirmed by comparing the jet width, $r_{0.95}$, on both sides of the jet after correcting for attenuation, where $r_{0.95}$ is the the radial location at which the time-averaged concentration is 5% of the centreline concentration at the same axial location, i.e., the solution to

$$\frac{\Theta(x, r_{0.95})}{\Theta(x, 0)} = 0.05. \tag{2}$$

The average difference of the magnitude of $r_{0.95}$ between both sides (i.e. the "top" and "bottom") of the jet was 0.43%.

Further details of the experiment, including measurements of the in-flow conditions and specifications of each individual camera, are provided by Lau and Nathan (2014).

3. Processing methodology

Figures 3a and 3b present an example of a mean (time-averaged) image of particle concentration, $\mathbf{I_{mean}}$, and an instantaneous image of particle concentration, $\mathbf{I}$, respectively. Here, the boldface notation refers to two-dimensional arrays. These images are consistent with others in the literature (Birzer et al., 2011a, 2012) in showing

Imaging region	Measurement axial extent (mm)	Probe dimensions (μm)	$\tilde{N}_p$	Θ (mm^{-3})	Δ_p (μm)	$\tilde{P}_{>1}$ (%)
A	0-51	$50.1 \times 50.1 \times 350$	≈ 0.084	≈ 96	≈ 219	4.2
B	40-240	$104.2 \times 104.2 \times 350$	≈ 0.171	≈ 45	≈ 281	8.3
C	230-400	$106.3 \times 106.3 \times 350$	≈ 0.083	≈ 21	≈ 362	4.1

Table 2: Details of the imaging system. For description of symbols, refer to the caption of table 1.
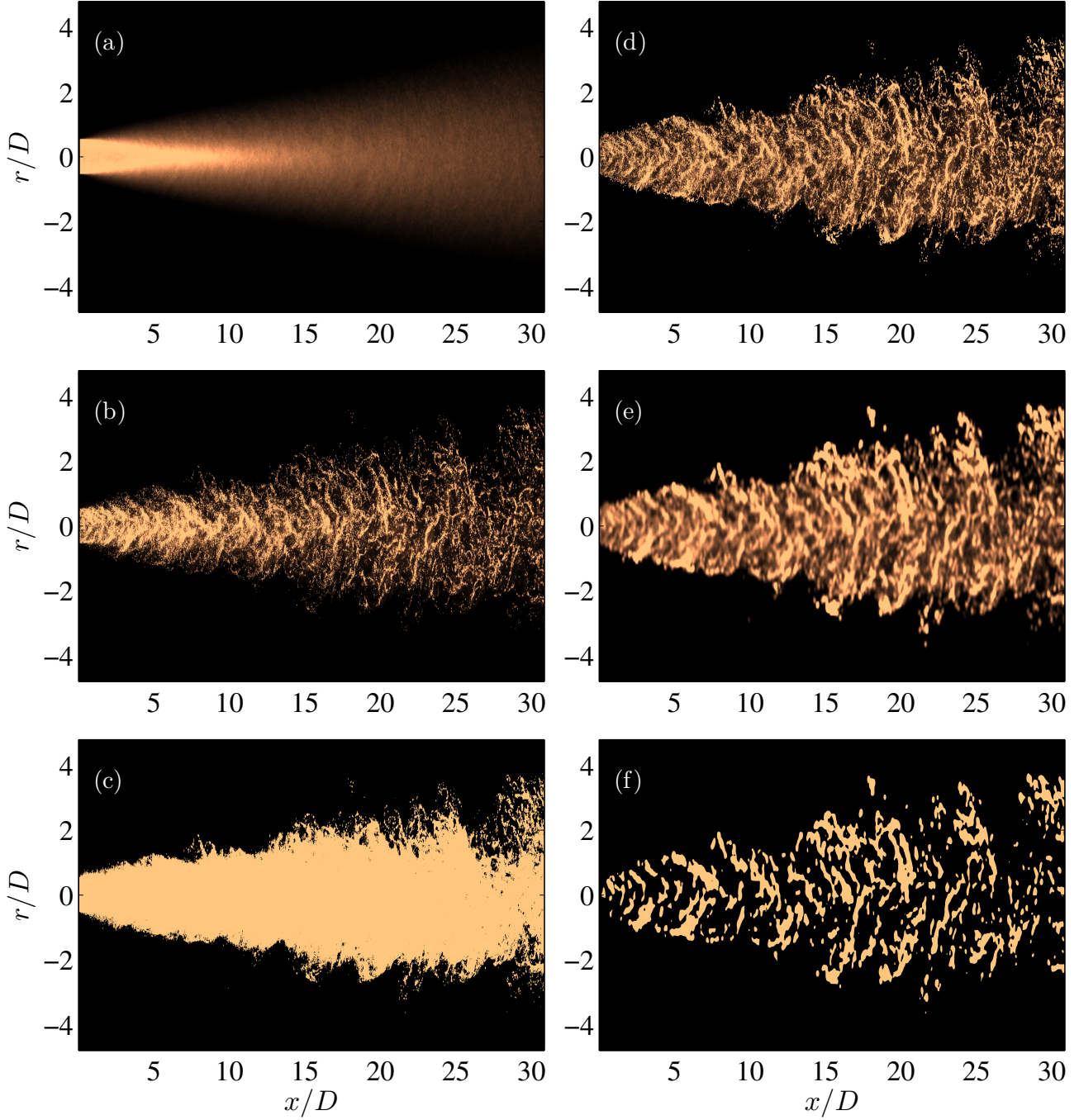
Figure 3: Images illustrating the steps involved in the present cluster determination methodology: (a) mean image (corrected for attenuation), $\mathbf{I_{mean}}$, (b) instantaneous image (corrected for attenuation), $\mathbf{I}$, (c) mask of concentration exceeding noise, $\mathbf{M_{sig}}$, (d) normalised intensity distribution, $\mathbf{I_{norm}}$, (e) normalised and smoothed intensity distribution, $\mathbf{I_{norm,s}}$ and (f) final binary cluster mask, $\mathbf{M_{clus}}$.

that the instantaneous particle distributions are very different from the mean. The inhomogeneities in the instantaneous particle distributions are evident right from the pipe exit plane, suggesting that particle clusters are generated within the pipe. These particle clusters propagate downstream, influencing the ongoing evolution of inhomogeneus particle distributions throughout the jet. The inhomogeneity is augmented by entrainment of the particle-free co-flow as the jet propagates downstream. The images of the cluster slices (denoting the planar slice through the three-dimensional clusters) appear to resemble filament-like structures which are stretched, reoriented and convoluted by the flow as they are convected downstream. Hence, the characterisation of these cluster slices requires a robust and flexible tool with which to extract consistent data across this wide range of features.

3.1. Cluster identification

Particle clusters, here broadly defined as localised regions of high instantaneous particle number density relative to the mean (time-averaged) number density due to non-random preferential concentration, were identified by extending the framework first proposed by Birzer et al. (2011b) and subsequently utilised in a number of studies of particle-laden turbulent jets (Birzer, 2012; Birzer et al., 2011a, 2012). In this method, a binary mask $\mathbf{M_{clus}}$ identifying cluster slices is produced for each instantaneous image using the difference between the mean ($\mathbf{I_{mean}}$) and instantaneous images ($\mathbf{I}$), utilising smoothing across a user-defined length scale L_s and applying a threshold. This method shares some similarity to the method utilised by Villermaux and Duplat (2006) in a study of scalar mixing in stirred tanks, although they applied the method to determine a coarse grained length scale rather than to identify clusters of scalars.

Unlike Birzer et al. (2011b), the current smoothing is performed on the ratio between $\mathbf{I}$ and $\mathbf{I_{mean}}$. Furthermore, while Birzer et al. utilises the mean concentration as the threshold, the current methodology utilises a thresholding scheme that follows Monchaux et al. (2010) in their study of particle clustering in homogeneous isotropic turbulence using Voronoï analysis described below. This process is then repeated for all instantaneous images.

The proposed method of cluster identification necessarily relies on the selection of a smoothing length scale L_s. This requirement, either through smoothing and/or binning, also appears in other methods that attempt to quantify particle clustering such as methods utilising box counting (Aliseda et al., 2002; Fessler et al., 1994; Hogan and Cuzzi, 2001; Rouson and Eaton, 2001; Wang and Maxey, 1993), Minkowski functionals (Calzavarini et al., 2008) and the radial/angular distribution function (Gualtieri et al., 2009; Salazar et al., 2008). As the choice of L_s will influence the identification and quantification of a cluster slice, the method is dependent upon this chosen length scale. Nevertheless, this is not necessarily a disadvantage because it allows the smoothing parameter to be systematically
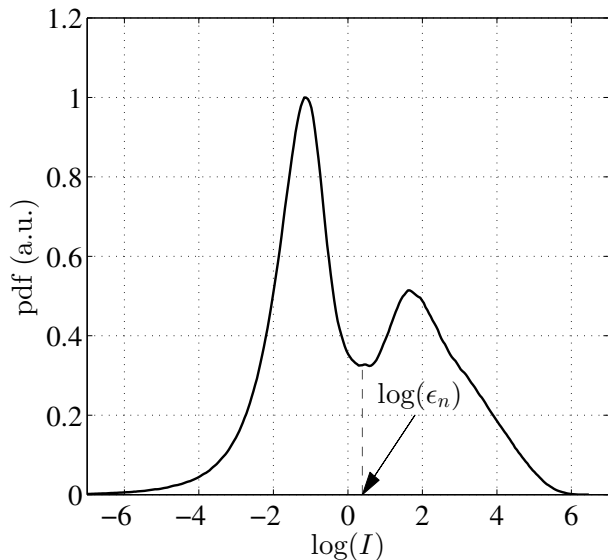

Figure 4: Probability density functions of $\log(I)$. Here I is the ensemble of individual pixel intensity values of instantaneous image $\mathbf{I}$. A double-peak profile is observed in the distribution of $\log(I)$ because the magnitude of measured signal (from Mie scattering off particles) is significantly higher than the (electronic) noise.

varied to preferentially assess clusters of a given length scale (Monchaux et al., 2012) or to determine the preferred length scales within the flow of interest (e.g. Villermaux and Duplat, 2006). In the current study, the latter method is used to select a single, unambiguous smoothing length scale, as is discussed in section 3.2.

To illustrate the cluster slice identification process, a single instantaneous image $\mathbf{I}$, as shown in figure 3b, is used as an example.

Firstly, a binary image mask is employed to remove the "noise" from the "signal", $\mathbf{M_{sig}}$, using the commonly used global histogram thresholding technique (Jähne, 1997). This is done by first plotting the probability density function (pdf) of the intensity values of the entire single image $\mathbf{I}$ on a logarithmic scale, as shown in figure 4. For each image, the pdf comprises a bi-modal distribution that can be approximated by the superposition of two Gaussian distributions. The lower intensity Gaussian distribution represents the distribution of "noise" (mostly electrical and electronic), while the higher intensity Gaussian distribution is the "signal" from the particles. The signal can be separated from the noise based on a threshold ϵ_n, which is taken to be the location of the minimum between the two peaks (see figure 4). Although the removal of the noise also results in the loss of some signal, this is insignificant because the signal is typically significantly larger than the noise. The resulting signal mask, $\mathbf{M_{sig}}$ (figure 3c), is thus used to reject any noise before further processing.

Next, the instantaneous image is normalised by the mean and subsequently multiplied by $\mathbf{M_{sig}}$, i.e., $\mathbf{I_{norm}} = (\mathbf{I} \oslash \mathbf{I_{mean}}) \circ \mathbf{M_{sig}}$ where the operators $\oslash$ and $\circ$ refer to element-wise division and multiplication (Hadamard prod-

7

uct), respectively. The use of $\mathbf{M_{sig}}$ prevents pixels in regions near to the jet edge from returning artificially high values, where the normalising values would be close to zero. The normalised image will be used to determine regions of high local particle concentration relative to the time-averaged particle concentration. Furthermore, this normalisation also facilitates a direct comparison of particle clustering in the current jet with flows with a uniform mean concentration, such as homogeneous isotropic turbulence. The normalised image $\mathbf{I_{norm}}$ is shown in figure 3d.

The normalised image is then smoothed using a two-dimensional spatial filter $\mathbf{f}$ of characteristic smoothing length L_s to obtain $\mathbf{I_{norm,s}}$ (figure 3e). Following Birzer et al. (2011b), we utilise a circular Gaussian filter whose elements can be expressed as

$$f_{m,n} = \exp\left[-8\left(\frac{m^2}{L_s^2} + \frac{n^2}{L_s^2}\right)\right] \quad (3)$$

where m is the array index in the x direction, n is array index in the r direction, and L_s is the smoothing length scale. Following this, the elements of the smoothed image $\mathbf{I_{norm,s}}$ are

$$[I_{norm,s}]_{i,j} = A \sum_{m=-\delta}^{\delta} \sum_{n=-\delta}^{\delta} f_{m,n} [I_{norm}]_{i-m,j-n} \quad (4)$$

where

$$A = \left(\sum_{m=-\delta}^{\delta} \sum_{n=-\delta}^{\delta} f_{m,n}\right)^{-1}.$$

Here, i and j are the array indices in the x and r directions, respectively, and $\delta = L_s/2$ is the limit to the size of the smoothing kernel.

The cluster mask is next obtained by applying a threshold ϵ_t to the smoothed image $\mathbf{I_{norm,s}}$, where the value of ϵ_t is obtained using the thresholding scheme proposed by Monchaux et al. (2010). In this scheme, the measured probability distribution of the normalised particle concentration is compared with the expected probability distribution of a field of randomly distributed particles (of equivalent bulk concentration). More specifically, this is done by comparing the the pdf of the ensemble of $I_{norm,s}$ with a Poisson distribution of the following standard deviation (Aliseda et al., 2002)

$$\sigma_P = \frac{\kappa}{L_s}\left(\frac{\pi}{4}\right)^{0.5} \left(\tilde{N}_p\right)^{-0.5}, \quad (5)$$

as shown in figure 5. Here, $\tilde{N}_p$ is the average (bulk) number of particles per pixel in the region of interest and $\kappa \approx 1.09$ is a correction factor to account for the non-uniform weighting of pixel values by the Gaussian filter, which was calculated numerically. For a uniform circular filter, $\kappa = 1$. The threshold value, ϵ_t, corresponds to the upper intersection between the two distributions
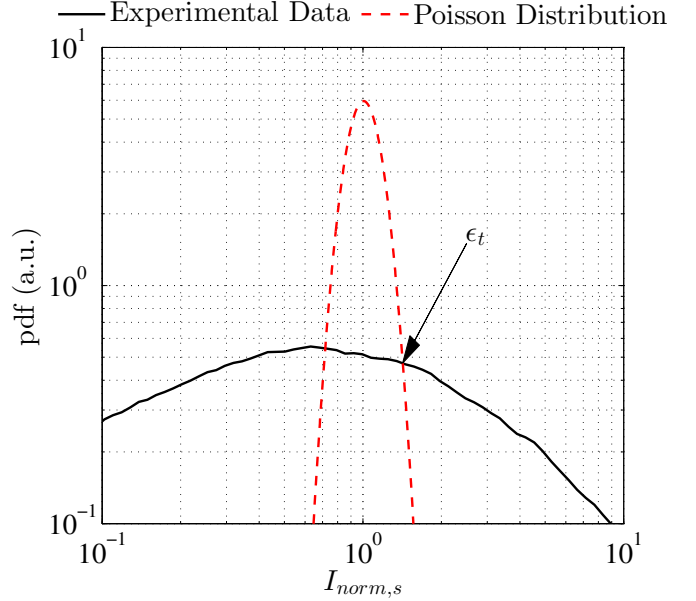

Figure 5: Probability density functions of $I_{norm,s}$. Here $I_{norm,s}$ is the ensemble of individual pixel intensity values of instantaneous image $\mathbf{I_{norm,s}}$. Also shown is the probability density function of the particle concentration calculated from a random Poisson process. The value ϵ_t is the threshold for determining particle clusters.

(see figure 5), following the method used by Monchaux et al. (2010). This contrasts the method of Birzer et al. (2011b), in which the threshold is fixed at $\epsilon_t = 1$. The benefit of the current method is that it provides a consistent, non-arbitrary threshold for cluster determination that is not sensitive to small fluctuations of particle concentration about the mean.

The cluster mask, $\mathbf{M_{clus}}$, is a binary image in which all values of $I_{norm,s} > \epsilon_t$ are set to unity and all other values set to zero. Individual cluster slices are then defined as any set of flagged pixels which are connected through any of its four non-diagonal neighbors (i.e. 4-connected). The cluster mask $\mathbf{M_{clus}}$ is shown in figure 3f.

A further optional step is introduced to avoid the erroneous detection of cluster slices that are artificially generated by the smoothing of isolated pixels of very high intensity within a region of low intensity. Because these signals may arise from individual particles that have been displaced outside the boundary of the jet, which is by definition, not a cluster, or from camera noise, these should be removed from the analysis. As the expected cluster area calculated from the smoothing of a single pixel is $A_{thres} = \pi L_s^2/4$, individual clusters with an area equal or less than this value is removed from further analysis.

Figure 6 presents the superposition of the instantaneous image $\mathbf{I}$ and the boundaries of the corresponding refined cluster mask $\mathbf{M_{clus}}$ as obtained using a smoothing length scale of $L_s = 0.25D$. These regions, identified by the algorithm as cluster slices, give good qualitative agreement with the images by visual inspection. Although subjective, reasonable qualitative agreement is an important compo-
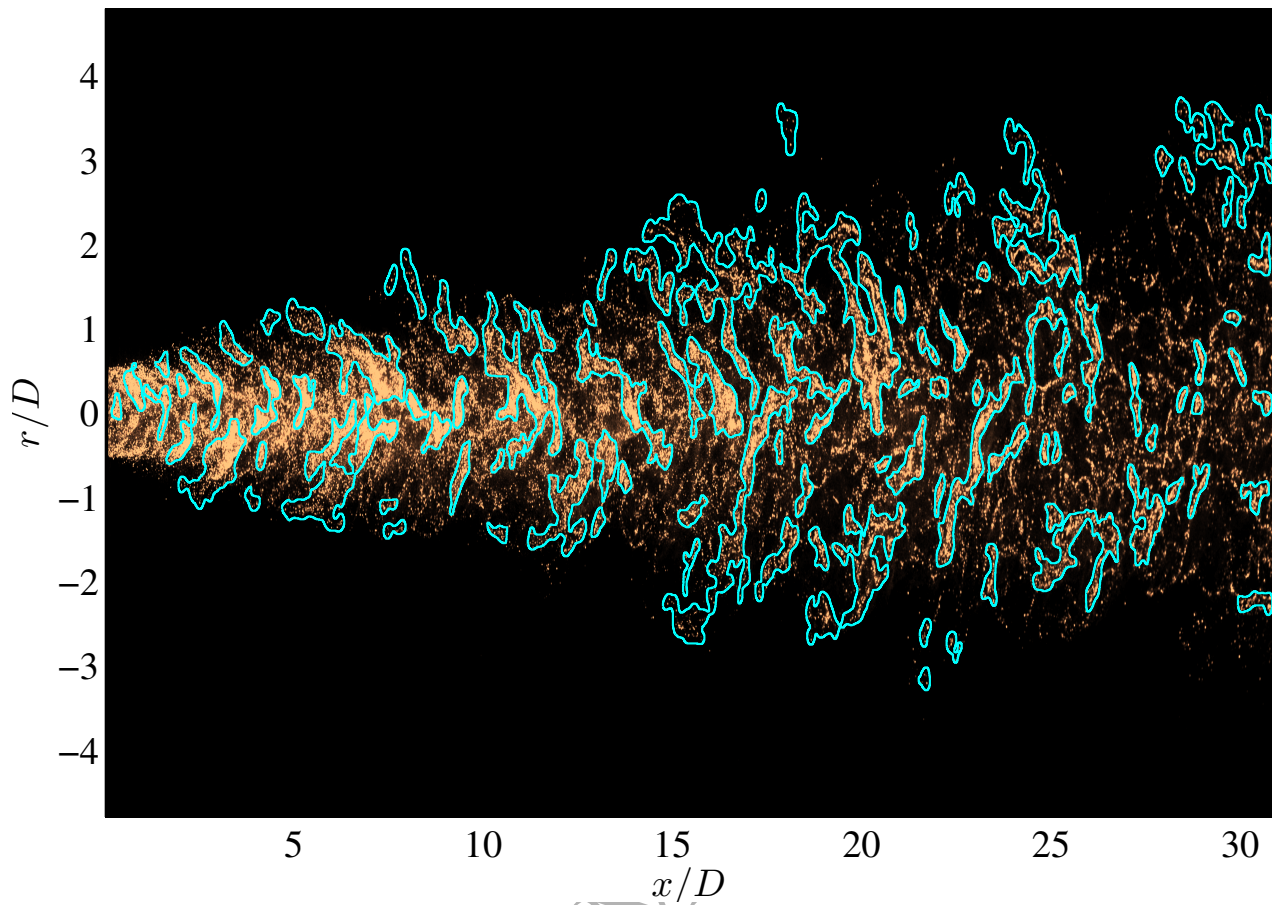
Figure 6: The superposition of the boundaries of cluster mask $\mathbf{M_{clus}}$ (cyan) with an instantaneous image $\mathbf{I}$. The cluster mask was obtained using a smoothing length scale of $L_s = 0.25D$.

nent of any image processing scheme. The results further show that clusters exist right from the jet exit and tend to be aligned at oblique angles to the jet axis when they emerge from the pipe, but that this angle reduces as the clusters propagate downstream.

3.2. Cluster analysis

Standard image processing techniques were used to calculate the area, A_c, and perimeter, P_c, of individual clusters (Jähne, 1997). Furthermore, as planar nephelometry from a mono-disperse particle size distribution directly provides a measurement of particle number density, the clusters identified using $\mathbf{M_{clus}}$ were used in conjunction with the instantaneous images, $\mathbf{I}$, to obtain the distribution of particle concentration within each cluster, Θ_c. From this, a measure of the magnitude of global clustering within a particular region was calculated from the relative proportion of particles residing within a cluster, i.e., $\chi = \overline{N_{p,in}/N_{p,tot}}$, where $N_{p,in}$ is the number of particles within clusters and $N_{p,tot}$ is the total number of particles, per image. A similar parameter has been used to study the effect of Stokes number on the degree of clustering at the exit of a turbulent jet (Lau and Nathan, 2016).

The influence of the smoothing length scale on the global clustering parameter χ within 5 different axial regions of the jet is presented in figure 7. It should be noted that the regions were limited to the region $x/D \leq 24$ because a significant proportion of the clusters further downstream were truncated by the downstream edge of the image. The effect of this truncation can be seen from the strong decline in χ as the smoothing length scale is increased beyond $L_s/D \gtrsim 0.5$ in the region $18 \leq x/D < 24$. Nevertheless the results reveal that χ exhibits a strong peak at $L_s/D \approx 0.25$. The peak value of L_s/D increases slightly with x/D from a value of about 0.25 close to the exit plane, to approximately 0.3 in the region $6 \leq x/D \leq 18$ and then decreasing again slightly with further increases in streamwise distance. This suggests that the length scale of the clusters is controlled primarily by the evolution inside the pipe and that the processes controlling their dimensions do not change greatly as the clusters propagate through the jet. Because the peak value of χ is almost independent of axial distance, the value of $L_s/D = 0.25$ was selected as the appropriate smoothing length scale for further analyses of cluster slices.
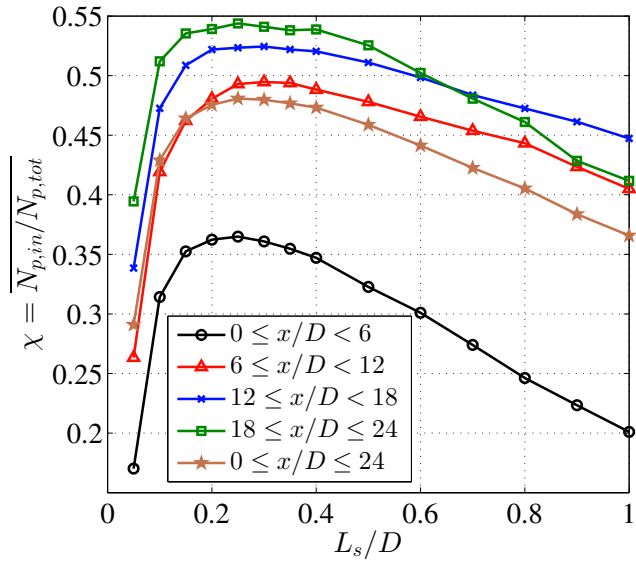
9

Figure 7: The distribution of the global clustering parameter, $\chi = \overline{N_{p,in}/N_{p,tot}}$, within 5 different axial regions as a function of the characteristic length scale of smoothing, L_s/D. Here, $N_{p,in}$ is the number of particles within clusters, and $N_{p,tot}$ is the total number of particles in an image.

3.3. Skeletonization method

A morphological skeletonization method in conjunction with a pruning algorithm was used to extract the characteristic dimensions of the cluster slices, including total length, $L_{c,skel}$ and width, $W_{c,skel}$. Morphological skeletonization, also known as a medial axis transform, produces an image skeleton consisting of a series of lines (of 1 pixel thickness) equidistant to the image boundaries (Blum, 1967), as shown in figure 8a. It should be noted that these image skeletons can also be generated from three-dimensional images (Borgefors et al., 1999), allowing the current method to be extended to three-dimensional measurements. These image skeletons are very useful shape analysis tools as they convey both topological and metric information, such as number of branches and loops, number of end-points, lengths of branches, and angles of branches (Russ, 2002; Soille, 1999). However, as the raw skeletons produced by this method are sensitive to small perturbations in the image boundary (Shaked and Bruckstein, 1998), a pruning method developed by Bai et al. (2007) was utilised to delete redundant skeleton branches, resulting in a pruned skeleton that represents the dominant features of the original image (see figure 8b). The strength of the method of Bai et al. is that it utilises global image information through discrete curve evolution to generate the pruned skeleton, and therefore has a low sensitivity to the differences in shapes and sizes of the cluster slice images.

The number of branches on each cluster slice was calculated by counting the number of pixels on the pruned skeleton which have 3 or more adjacent neighbors. Additionally, the length of the longest segment of the pruned

skeleton segment was used to estimate the characteristic length of the cluster slice, $L_{c,skel}$ (see figure 9). The characteristic width of the cluster slice was calculated based on a two step procedure. Firstly, a first-pass estimate of the cluster slice width was obtained by taking the average of $2d_{min,i}$, where $d_{min,i}$ is the distance between each point i on the skeleton and its nearest boundary. Next, each skeleton branch was then shortened by half this amount to produce a trimmed skeleton, as shown in figure 8c. The characteristic cluster slice width $W_{c,skel}$ is then the average of $2d_{min,j}$, where j is now each point on the trimmed skeleton. The benefit of calculating the object length and width using this method is that it is robust, i.e., it is independent of reference frame, object rotation and object curvature.

From the calculated cluster slice width, an inverse skeleton was produced for each image by applying a constant width of $W_{c,skel}$ to the trimmed, pruned skeleton. Two examples of inverse-skeletons are shown in figure 8c and figure 9. As can be seen, the inverse-skeleton shows strong resemblance to the boundary of the original cluster slice, and importantly, the calculated dimensions $W_{c,skel}$ and $L_{s,skel}$ can be interpreted as the characteristic width and length of the cluster slice. The area A_c, perimeter P_c, and location of the centroid relative to the origin, (x_c, r_c), of each individual cluster slice was calculated directly from the original cluster slice image.

The skeletonization method also provides the option to extract higher order data, such as distances between individual branch points, lengths of individual branches, angles between branches and the average radius-of-curvature. These measurements provide additional data about the structure of the turbulence associated with the given value of smoothing length scale, L_s. In addition to providing new insight, such data can also be compared with computational models to provide additional tests for validation, since numerical data sets can be processed in the same way.

3.4. Error analysis of cluster measurements

Following the methods of Qamar et al. (2011) and Chan et al. (2014), the accuracy with which the algorithm calculates the cluster slice dimensions $L_{c,skel}$ and $W_{c,skel}$ from the data was assessed by comparing these calculated values with independent values measured manually, $L_{c,man}$ and $W_{c,man}$, respectively, from a randomly-selected sample of 148 cluster slices. These manually calculated values were estimated by firstly identifying a line segment that most closely resembles the shape of the object through visual inspection and, secondly, by calculating both the length of this segment and the average distance of the closest boundary to this segment. The characteristic cluster slice lengths and widths calculated using the equivalent-ellipse method (Qamar et al., 2011), $L_{c,eq}$ and $W_{c,eq}$, and the bent-object algorithm (Chan et al., 2014), $L_{c,bent}$ and $W_{c,bent}$, respectively, are also included in the comparison. Importantly, these methods all estimate the cluster length
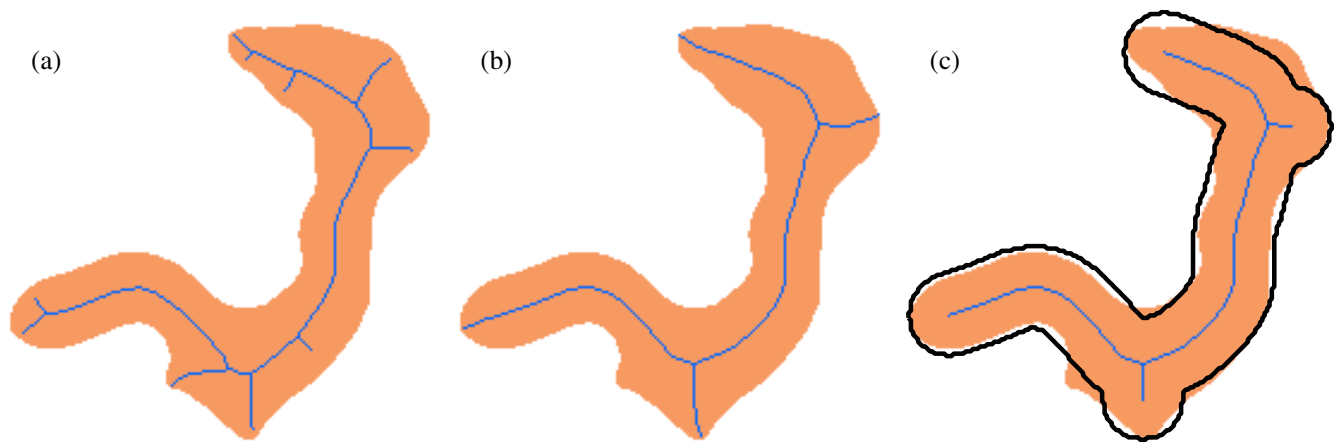
Figure 8: Images of cluster slices where the light blue line represents the (a) full (unpruned) skeleton (b) pruned skeleton and (c) trimmed, pruned skeleton. The black solid line represents the boundary to the inverse-skeleton.
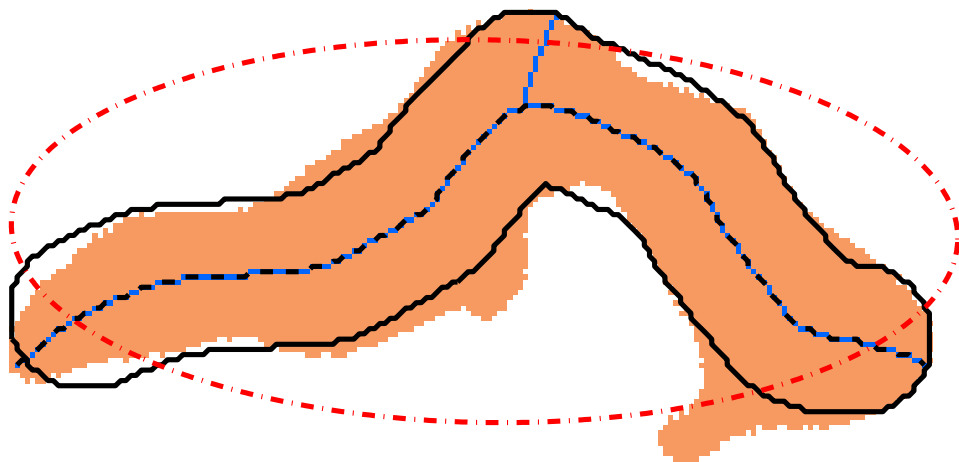

Figure 9: An example of a measured cluster slice with the equivalent ellipse (red dash-dot line), pruned skeleton (cyan line), longest segment (black dashed line) and inverse-skeleton (black solid line).
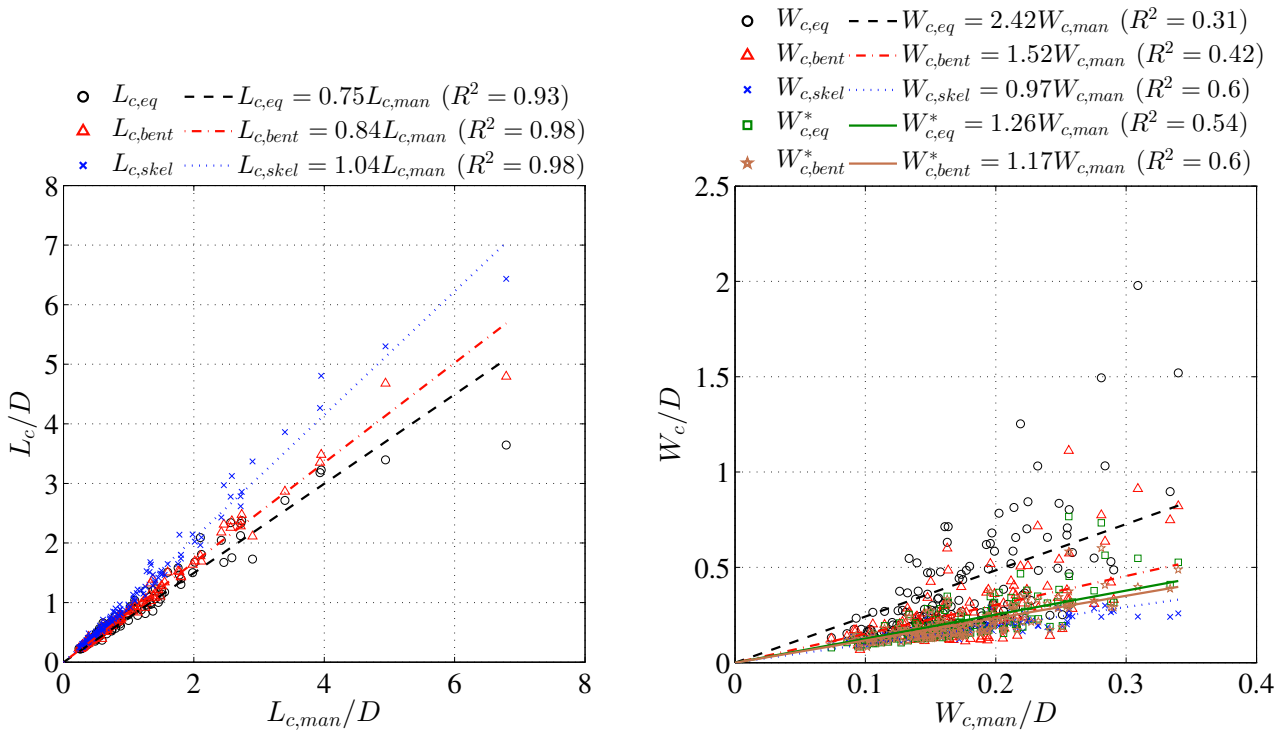
Figure 10: The statistical variation in the characteristic cluster slice length and width evaluated using the equivalent-ellipse method, $L_{c,eq}$ and $W_{c,eq}$, respectively, the bent-object algorithm of Chan et al. (2014), $L_{c,bent}$ and $W_{c,bent}$, respectively, and the current skeletonization method, $L_{c,skel}$ and $W_{c,skel}$, respectively, versus the manually-evaluated cluster slice length, $L_{c,man}$, and width, $W_{c,man}$. Also included are the pseudo-widths $W_{c,eq}^* = A_c/L_{c,eq}$ and $W_{c,bent}^* = A_c/L_{c,bent}$, which were calculated from the equivalent-ellipse and bent-object data, respectively.

in broadly the same way, i.e., by calculating the length of a continuous segment that most closely represents the "axis" of the object. Hence the different measures are all directly comparable. Nevertheless, it should be noted that these definitions of characteristic lengths are not absolute and different definitions of characteristic length may exist depending on the flow.

The results are shown in figure 10. Also shown are the pseudo-widths $W_{c,eq}^*$ and $W_{c,bent}^*$ which were calculated from the equivalent-ellipse and bent-object methods, respectively, by taking the ratio of the cluster slice area and length, i.e., $W_{c,eq}^* = A_c/L_{c,eq}$ and $W_{c,bent}^* = A_c/L_{c,bent}$. The results presented in figure 10 show that the cluster slice lengths calculated from all three methods have a high degree of linear correlation to $L_{c,man}$, with a co-efficient of determination of $R^2 = 0.93 - 0.98$. However, $L_{c,eq}$ and $L_{c,bent}$ typically underestimate the cluster slice length by $\approx 16 - 25\%$, while $L_{c,skel}$ on average, calculates the cluster slice length to within $\approx 4\%$. This is because both the equivalent-ellipse and Chan et al.'s bent-object methods calculate the cluster slice length using straight lines, which tends to underestimate lengths of curved objects, while the skeletonization method produces curved lines which more closely resemble the axes of cluster slices. The error in $L_{c,bent}$ estimated here is consistent with the results of Chan et al., who estimated that $L_{c,bent}$ predicts

the manually-evaluated lengths of soot sheets to $\approx 11\%$. The results also show that $W_{c,skel}$ is more strongly correlated to $W_{c,man}$, with $R^2 = 0.60$, than $W_{c,eq}$ and $W_{c,bent}$ ($R^2 = 0.31$ and $R^2 = 0.42$, respectively). Furthermore, the equivalent-ellipse method overestimates cluster slice width by more than a factor of two, $W_{c,bent}$ overestimates cluster slice width by $\approx 52\%$, and $W_{c,skel}$ underestimates cluster slice width by $\approx 3\%$. The large errors in $W_{c,eq}$ and $W_{c,bent}$ are due to the filament-like shapes of the cluster slices, which have thicknesses that are not well represented by either method. These errors are significantly higher than that found by Qamar et al. (2011), who estimated that both $W_{c,eq}$ and $L_{c,eq}$ approximate manually-evaluated soot sheet widths and lengths to within $\approx \pm 5\%$. The larger errors found here are due to the more irregular, branched, and wrinkled shapes of the current particle cluster slices than the soot sheets analysed by Qamar et al., for which $\approx 85\%$ were straight and non-branched. Interestingly, the pseudo-widths $W_{c,eq}^*$ and $W_{c,bent}^*$ are more accurate predictors of cluster slice width than $W_{c,eq}$ and $W_{c,bent}$, overestimating the manually-evaluated cluster slice width by only $\approx 17 - 26\%$ and showing a higher coefficient of determination of $0.54 \leq R^2 \leq 0.60$.

The cluster slice dimensions using all three methods were also calculated for the entire dataset consisting of 155,102 individual cluster slices, providing a sufficiently
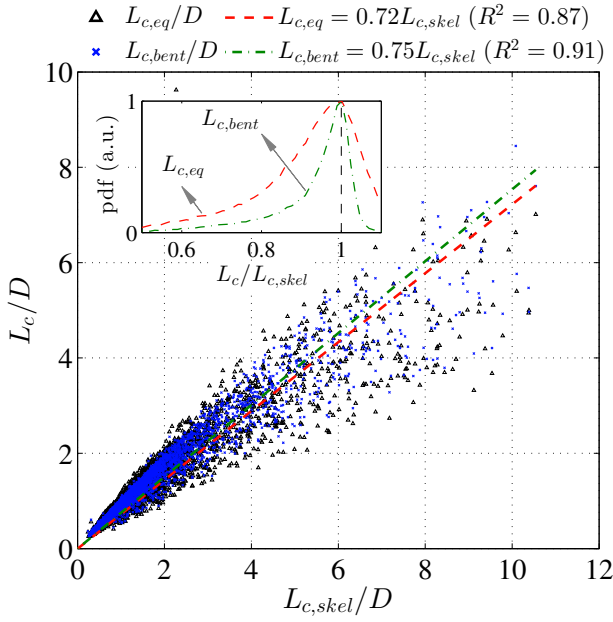
Figure 11: The cluster slice length measured using the equivalent-ellipse method, $L_{c,eq}$ and the bent-object method, $L_{c,bent}$, plotted against the cluster slice length calculated from the skeletonization method, $L_{c,skel}$. Note that only 10% of the data points were included in the figure for clarity.
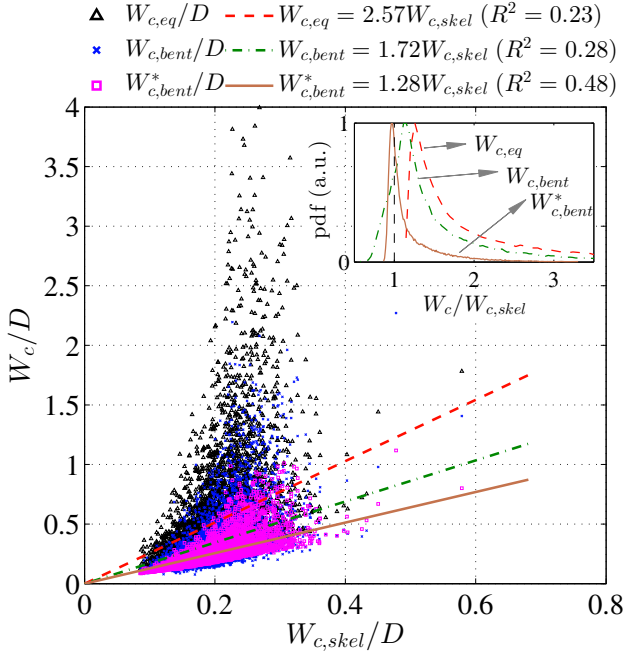

Figure 12: The cluster slice width measured using the equivalent-ellipse method, $W_{c,eq}$ and the bent-object method, $W_{c,bent}$, plotted against the cluster slice width calculated from the skeletonization method, $W_{c,skel}$. Also included is the pseudo-width $W^*_{c,bent} = A_c/L_{c,bent}$. Note that only 10% of the data points were included in the figure for clarity.

Parameter	Mean	Mode	Standard Deviation
$L_{c,eq}/L_{c,skel}$	0.72	1.00	0.138
$L_{c,bent}/L_{c,skel}$	0.75	1.00	0.109
$W_{c,eq}/W_{c,skel}$	2.57	1.26	1.585
$W_{c,bent}/W_{c,skel}$	1.72	1.15	0.873
$W^*_{c,bent}/W_{c,skel}$	1.28	0.96	0.377

Table 3: Statistical comparison between the cluster slice lengths and widths calculated using the equivalent-ellipse method, $L_{c,eq}$ and $W_{c,eq}$ respectively, the bent-object method, $L_{c,bent}$ and $W_{c,bent}$, respectively, and the skeletonization method, $L_{c,skel}$ and $W_{c,skel}$, respectively. Also included is the pseudo-width $W^*_{c,bent} = A_c/L_{c,bent}$ calculated using date from the bent-object method.

large sample size for statistical analysis. The mean computational time per cluster slice, relative to the computational time of the equivalent-ellipse method, T_{eq}, was found to be $T_{skel}/T_{eq} = 534$ and $T_{bent}/T_{eq} = 7.2$ for the skeletonization and bent-object methods, respectively. For a standard desktop computer with 4GB RAM and running a 3GHz Quad Core processor, this equates to $T_{skel} \approx 0.54$s per cluster slice.

The cluster slice length measured using the equivalent-ellipse and bent-object methods are plotted against $L_{c,skel}$ in figure 11. The results show that, on average, $L_{c,eq}$ and $L_{c,bent}$ are 28% and 25% lower than $L_{c,skel}$, respectively. More importantly, the probability density function of $L_{c,bent}/L_{c,skel}$ shows a narrower distribution than that of $L_{c,eq}/L_{c,skel}$ (see inset of figure 11). This implies that $L_{c,bent}$ is a more precise estimator of cluster slice length than $L_{c,eq}$.

Figure 12 presents the calculated widths $W_{c,eq}$, $W_{c,bent}$ and $W^*_{c,bent}$ as a function of $W_{c,skel}$. Consistent with the results presented in figure 10, $W_{c,eq}$, $W_{c,bent}$ and $W^*_{c,bent}$ all overestimate cluster slice width, with $W^*_{c,bent}$ being most closely correlated to $W_{c,skel}$. Furthermore, the pdf of $W^*_{c,bent}/W_{c,skel}$ shows a narrower distribution, with a peak at $W^*_{c,bent}/W_{c,skel} \approx 0.96$. By comparison, the peak of $W_{c,eq}/W_{c,skel}$ and $W_{c,bent}/W_{c,skel}$ occur at ≈ 1.26 and ≈ 1.15, respectively. These results are summarised in table 3.

The results presented here clearly show that the skeletonization method provides significantly more accurate and consistent measurements of cluster slice dimensions that either the equivalent-ellipse or the bent-object method, measuring the cluster slice length and width to within $\approx 4\%$ of the manually-evaluated values. It should be reiterated, however, that the lengths and widths measured using all these methods are intended as a measure of the *characteristic* dimensions of the cluster slices, and do not represent an absolute measure of the cluster slice length and width, respectively. The skeletonization method is also significantly more computationally intensive than these other two methods. Therefore, for applications which require rapid processing at the expense of accuracy, such as real-time analysis, the bent-object method
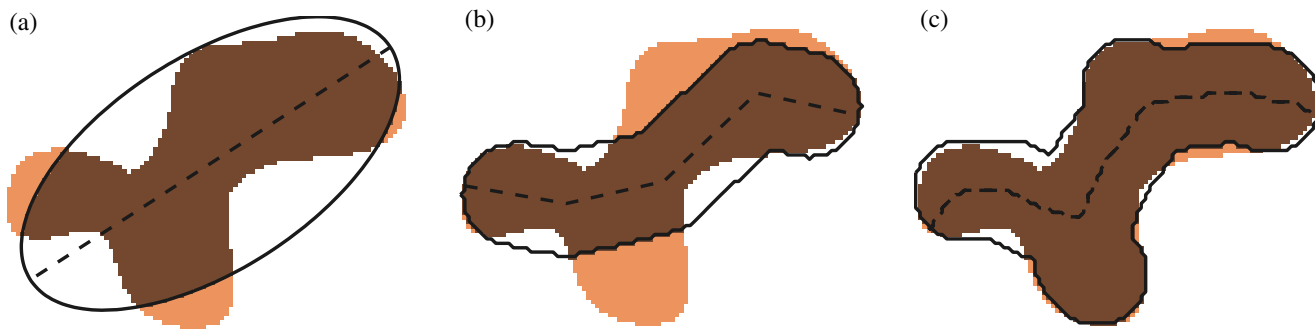
Figure 13: The inverse shapes (black line) and intersecting areas (dark brown) calculated from a single cluster slice image using a) the equivalent-ellipse, b) bent-object and c) skeletonization methods. In this example, the pseudo-area-ratio values for each method were calculated as $\lambda_{c,eq} = 0.774$, $\lambda_{c,bent} = 0.792$ and $\lambda_{c,skel} = 0.934$, respectively.

may be a viable alternative, with $L_{c,bent}$ and $W^*_{c,bent}$ measuring cluster slice dimensions to within $\approx 17\%$.

A further comparison of the accuracy of the three automated methods of measuring cluster slice dimensions was obtained by comparing the "inverse shape", i.e. the actual shape derived from each method, with the shape of the original cluster slice. These inverse shapes are the ellipse of the equivalent-ellipse method and the inverse-skeleton of the current skeletonization method. The inverse shape of the bent-object algorithm is a bent object with a constant thickness, $W_{c,bent}$. A typical example of these inverse shapes is presented in figure 13. A statistical comparison of these inverse shapes with their respective original was then obtained from a comparison of the pseudo-area with the real area, $\lambda_c = A_{c,int}/\sqrt{A_c A_{c,inv}}$, where $A_{c,int} = A_c \cap A_{c,inv}$ is the intersecting area between the original cluster slice image and the inverse shape, as illustrated in figure 13. Here, A_c and $A_{c,inv}$ are the areas of the original and inverse cluster slice images, which was calculated by summing the number of pixels in each image, respectively. For cases where the inverse shape exactly traces the perimeter of the measured cluster slice, $\lambda_c = 1$.

Figure 14 presents the probability density function λ_c for the entire dataset. The results show that the skeletonization method produces the most consistent measurements, with a narrow distribution of λ_c values peaking at $\lambda_c \approx 0.89$. The average value of λ_c for each method are $\overline{\lambda}_{c,eq} = 0.84$, $\overline{\lambda}_{c,bent} = 0.80$ and $\overline{\lambda}_{c,skel} = 0.89$, respectively. This is further evidence that the skeletonization method characterises the dimensions of these complex shapes more accurately than do the equivalent-ellipse and bent-object methods. Interestingly, the equivalent-ellipse method outperforms the bent-object method in estimating the cluster slice shape. Nevertheless, the broad distribution of λ_c values for both the equivalent-ellipse and bent-object methods indicates the inability of these methods to accurately
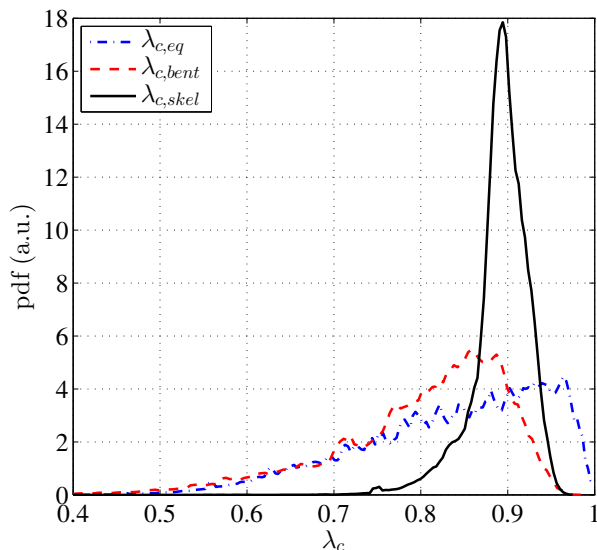

Figure 14: The probability density function of the pseudo-area-ratio term λ_c, calculated for all three cluster characterisation methods.

portray the more complex shapes of the present cluster slice images.

4. Case study

The skeletonization method of cluster measurement was applied to the full dataset of 155,102 individual cluster slices identified using a single smoothing length scale of $L_s = 0.25D$. This smoothing length scale was selected because it has been shown to result in a peak in the magnitude of clustering within the jet, as previously discussed in section 3.2. In this case study, only cluster slices of area $A_c > \pi L_s^2/4$ were selected for analysis, as suggested in section 3.1. From the values of cluster slice length
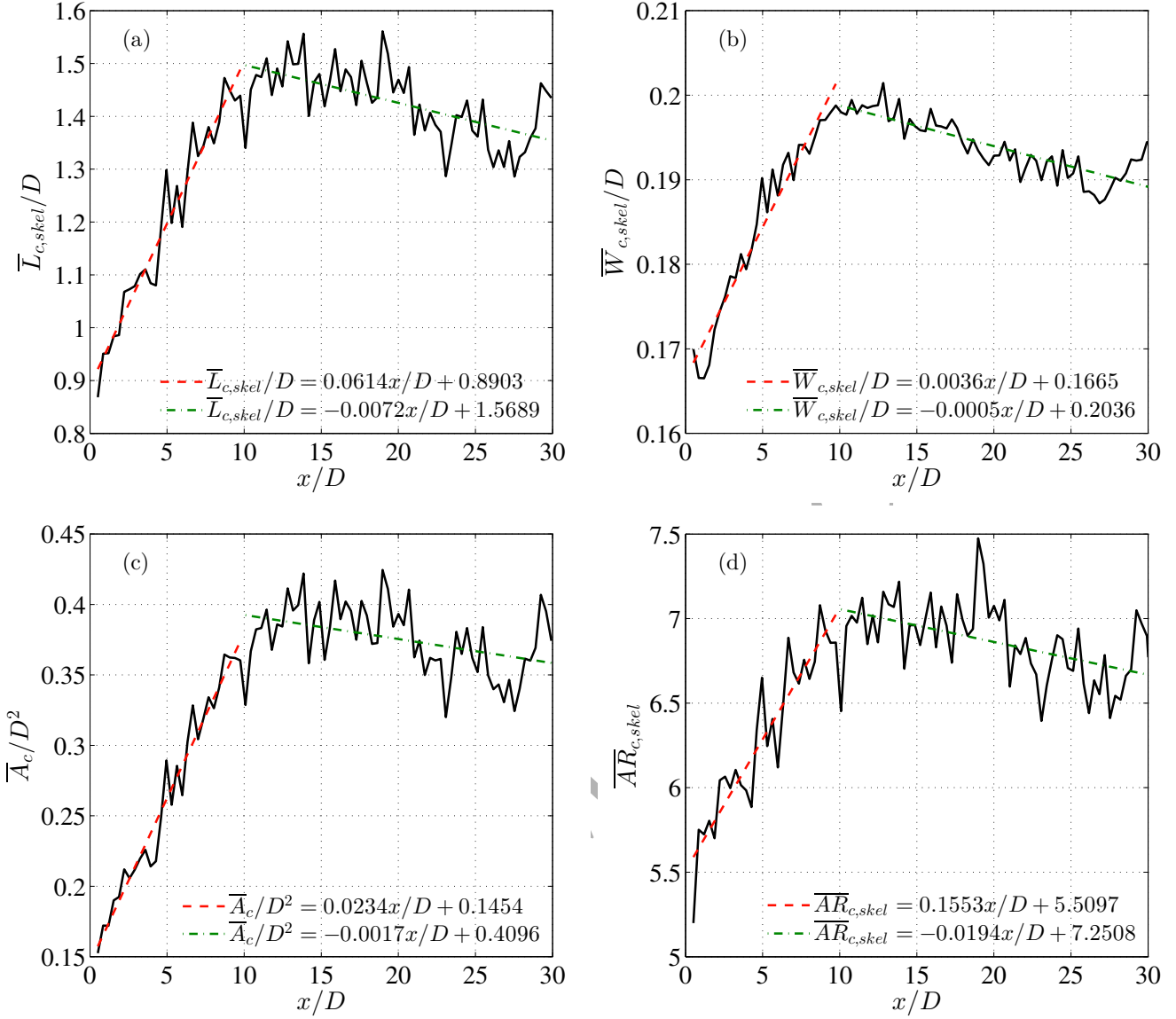
Figure 15: The axial evolution of the radial-mean cluster slice length, $\overline{L}_{c,skel}/D$, width, $\overline{W}_{c,skel}/D$, area, $\overline{A}_c/D^2$ and aspect ratio, $\overline{AR}_{c,skel}$.

and width, the cluster slice aspect ratio was calculated as $AR_{c,skel} = L_{c,skel}/W_{c,skel}$. All of the data were then binned at 90 fixed intervals in the axial direction, and subsequently the average, denoted by the overbar, and standard deviation, denoted by σ, was calculated for each bin.

Figure 15 presents the axial evolution of the normalised radial-mean cluster slice length $\overline{L}_{c,skel}/D$, width, $\overline{W}_{c,skel}/D$, area $\overline{A}_c/D^2$ and aspect ratio $\overline{AR}_{c,skel}$. In general, throughout the jet the characteristic cluster slice lengths are on order of the pipe diameter, D, while the average characteristic cluster slice width is narrowly distributed in the range $0.17 \lesssim \overline{W}_{c,skel}/D \lesssim 0.2$, although it should be noted that these values are dependent on the choice of L_s. The large cluster slice length-to-width ratio results in a typical cluster slice aspect ratio of $AR_{c,skel} \approx 6 - 7$, consistent with the initial visual observation that

the cluster slices tend to form long, filament- or sheet-like structures (figure 6).

The non-zero value of $\overline{L}_{c,skel}/D$ at $x/D \approx 0$ is further evidence that particle clusters are found at the jet exit, implying that the phenomenon of clustering occurs within the pipe as previously discussed in section 3.1. Furthermore, the observation that the average cluster slice lengths at the exit is $\overline{L}_{c,skel}/D \approx 1$, combined with the earlier observation that they are typically aligned at oblique angles to the jet axis (see also figure 6), suggests that the length of the clusters, as they are formed within the pipe, is limited by the pipe diameter. Given the deduction of Aliseda et al. (2002) that a cluster may exhibit the behaviour of a large "pseudo-particle" that responds only weakly to the flow, this suggests that the influence of these clusters propagates downstream through a "memory" that is greater than that
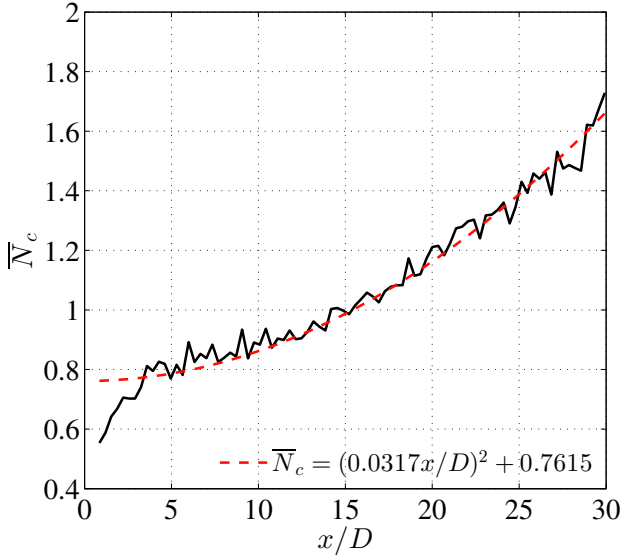
15

Figure 16: The axial evolution of the average number of cluster slices (per bin), $\overline{N}_c$.

of the single phase flow.

The cluster widths measured here vary over the range $0.17 \lesssim \overline{W}_{c,skel}/D \lesssim 0.2$, which is some 20-32% less than the value of smoothing length scale that corresponds to peak global clustering, $L_s/D = 0.25$ (section 3.2). As this value of L_s/D is expected to over-estimate the characteristic clustering length scale due to the use of a Gaussian smoothing function which utilises weighting values that decrease progressively with increased distance from the centre of the function, this suggests that the preferred clustering length scale within the current flow is $\approx 0.17D$. This is at least an order of magnitude lower than the estimated Kolmogorov length scale (Antonia et al., 1980; Eggels et al., 1994), and an order of magnitude smaller than the pipe diameter. This suggests that clustering may occur preferentially at a small range of intermediate length scales of the flow.

The results also show that the characteristic cluster slice length, width and area increases linearly with axial distance in the near field, $0 \leq x/D \lesssim 10$, consistent with the observations made in section 3.2. This growth in cluster size is attributed to the overall expansion of the jet and entrainment of the unseeded co-flow. In the first 10 diameters downstream of the jet exit the cluster slice length increases by $\approx 69\%$, the cluster slice width increases by $\approx 22\%$, while $r_{0.95}$, which is a measure of the jet width (see equation 2), increases by $\approx 156\%$. As the axial growth rate of the cluster slice length is greater than the width, the cluster slice aspect ratio, $\overline{AR}_{c,skel}$, also grows within this region. The high axial growth rate of the cluster slice length (relative to width) in the near-field of the jet exit suggests that the growth rate of the cluster lengths are "stunted" within the pipe, consistent with the cluster lengths being limited by the pipe diameter within the pipe

as previously discussed. As the cluster widths are smaller than the pipe diameter, this phenomenon does not affect the growth of the cluster slice widths. For $x/D \gtrsim 10$, the cluster slice length, width and area decrease slightly with axial distance. Interestingly, within this region, the axial decay rate of cluster slice length and width is similar, resulting in an approximately constant value of $AR_{c,skel} \approx 7$, although it should be re-iterated that this value may depend on the choice of smoothing length scale, L_s. The near-field peak in these values at $x/D \approx 10$ is consistent with the time-averaged centreline concentration profile, which exhibits a similar trend (see figure 3a and also Lau and Nathan, 2014). However, the axial location of this transition between a cluster growth mode to a cluster shrinkage mode is slightly further downstream from the exit than the location of the peak centreline concentration of the mean flow, which occurs at $x/D \approx 6$. Together, these results show that the axial growth rate and decay of particle concentration within clusters is significantly lower than in mean the jet, which indicates that particle diffusion within clusters is smaller than that in the mean particle-laden flow.

Figure 16 presents the average number of cluster slices (per bin), $\overline{N}_c$, as a function of the axial distance. This shows that the average number of cluster slices across the jet increases monotonically as a function of x^2. As the cross-sectional area of the jet is proportional to x^2 for a jet that expands linearly with axial distance, it then follows that the average number of clusters per volume is approximately constant in the current two-phase jet.

Figure 17 presents the normalised standard deviation of the cluster slice length and width, $\sigma_{Lc,skel}/\overline{L}_{c,skel}$ and $\sigma_{Wc,skel}/\overline{W}_{c,skel}$, respectively, as a function of axial distance from the jet exit. These measurements should be interpreted with some caution, as they not only may represent true fluctuations in the size of the clusters, but owing to the use of planar measurements may also arise from the out-of-plane motion of the three-dimensional clusters. Nevertheless, the normalised standard deviations for cluster slice length increase with axial distance. This is consistent with previous concentration measurements in single-phase jets, which show that the scalar fluctuations increase with axial distance from the jet exit (Mi et al., 2001). Furthermore, the larger values of $\sigma_{Lc,skel}/\overline{L}_{c,skel} \approx 0.7 - 1.2$ compared to $\sigma_{Wc,skel}/\overline{W}_{c,skel} \approx 0.21 - 0.25$ is consistent with the observation that the cluster slices form filament-like structures. On the other hand, the relatively small values of $\sigma_{Wc,skel}/\overline{W}_{c,skel}$ throughout the jet is further evidence that the measured mean cluster slice widths are representative of a dominant flow length scale (as previously discussed). More specifically, the small values of $\sigma_{Wc,skel}/\overline{W}_{c,skel}$ also suggest that the mean cluster slice width measured at the jet exit, $\overline{W}_{c,skel}/D \approx 0.17$, is representative of a length scale upstream of the jet exit (i.e. within the pipe). The source and nature of this length scale is currently unknown. Further measurements of the turbulent two-phase flow within a pipe is required to elu-
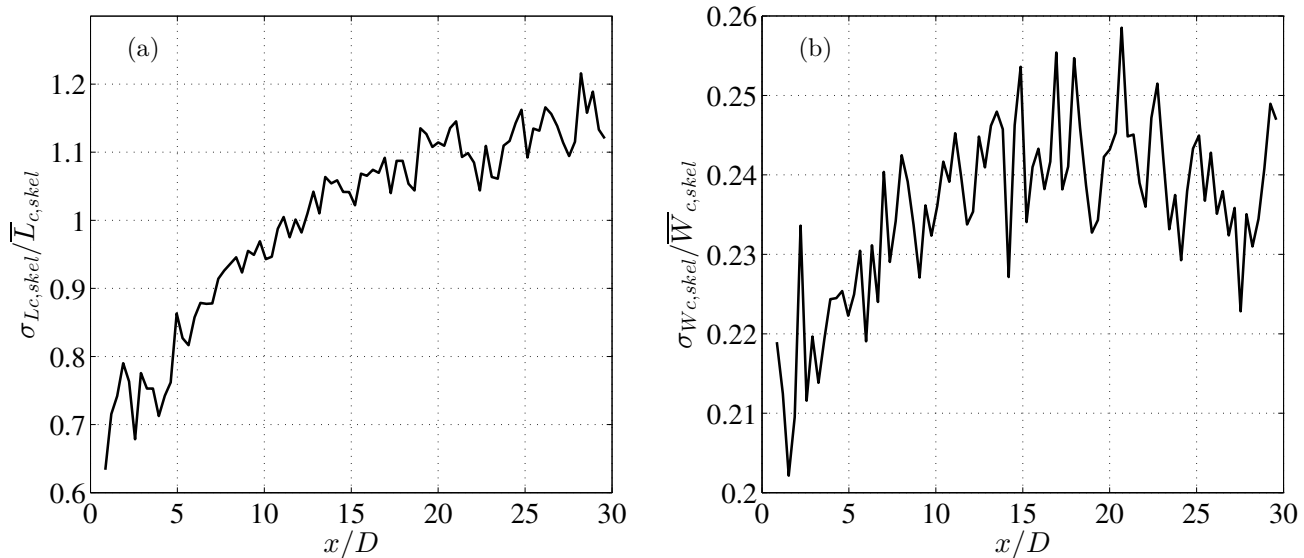
16

Figure 17: The axial evolution of the normalised radial standard deviation of the cluster slice length $\sigma_{Lc,skel}/\overline{L}_{c,skel}$, and width, $\sigma_{Wc,skel}/\overline{W}_{c,skel}$.

cidate this phenomenon.

5. Conclusions

A novel approach to reliably quantify from two-dimensional images the characteristic dimensions of particle clusters with highly irregular, complex, and branched shapes in a two-phase jet has been developed using image processing that includes a morphological skeletonization and pruning algorithm. The measurements from this automated method correlates very well with a manual assessment of 148 different cluster slices, with R^2 values for the measured lengths and widths being $R^2 = 0.98$ and $R^2 = 0.60$, respectively. This technique has been shown to measure the characteristic length and width of two-dimensional slices through three-dimensional clusters to within $\approx 4\%$ of manually determined values. This is a substantial improvement on the previously reported equivalent-ellipse (Qamar et al., 2011) and bent-object (Chan et al., 2014) methods, which measure the comparable length of cluster slices to within $\approx 16 - 25\%$, and the comparable width of cluster slices to within $\approx 52 - 242\%$ when applied to the current two-phase jet, although it requires significantly more computational expense. Furthermore, this technique has also been shown to more accurately and consistently capture the shape of the identified cluster slices than the equivalent-ellipse and bent-object methods.

The current method for identifying slices through clusters, which is a refinement of the method previously proposed by Birzer et al. (2011b), does not require the identification of individual particles within the flow. Therefore, the current method can be applied more generally to densely seeded flows where two- and four-way coupling is

important, expanding upon the current capability of cluster measurement which has typically been limited to dilute flows. Additionally, the current method avoids the need for an arbitrary threshold as it utilises a robust and unambiguous thresholding scheme based on the method proposed by Monchaux et al. (2010). These developments provide more consistent and accurate identification of cluster slices as they take into account variations in intensity and concentration between individual instantaneous images. The method for extracting cluster dimensions utilises the existing methods of image skeletonization (Jähne, 1997) and skeleton pruning (Bai et al., 2007), which are widely employed in computer science and machine vision applications, but have not previously applied to the analysis of particle clusters.

The application of this overall method to a particle-laden jet with a Stokes number of $Sk_D = 1.4$ and Reynolds number of $Re_D = 10,000$ revealed that the magnitude of global clustering, as measured by the parameter χ, displays a peak corresponding to $0.25 \lesssim L_s/D \lesssim 0.3$. An assessment of the dimensions of cluster slices utilising a fixed smoothing length scale $L_s/D = 0.25$ showed that the average sliced cluster widths were narrowly distributed in the range $0.17 \lesssim \overline{W}_{c,skel}/D \lesssim 0.2$. This is an order of magnitude smaller than the pipe diameter and at least an order of magnitude larger than the estimated Kolmogorov length scale. Together, these results suggest that clusters are generated inside the pipe at preferred length scales corresponding to intermediate length scales of the flow.

The results also showed that the average sliced cluster length at the pipe exit is $\overline{L}_{c,skel}/D \approx 1$. That the lengths of the sliced clusters is close to the pipe diameter and that they are aligned at oblique angles to the pipe axis suggests that these clusters are formed by coherent structures

within the pipe that span the entire pipe diameter, which limits their length. The measurements also show that the cluster slice aspect ratio is typically very high, $AR \approx 6-7$, consistent with the observation that clusters, as detected by a two-dimensional imaging system, are typically in the form of long, thin filaments.

Measurements of the axial evolution of the cluster slice dimensions demonstrate that the radial-mean sliced cluster length peaks at $x/D \approx 10$, which is slightly further downstream than the location of the peak time-averaged centreline concentration, which occurs at $x/D \approx 6$. The measurements also show that the axial growth of both the mean sliced cluster length and width are significantly lower than the axial expansion of the jet. Together, these results indicate that particle diffusion within clusters is slower than the mean flow. Additionally, the measurements also show that the average number of cluster slices increases quadratically with axial distance, which, for a jet that linearly expands with axial distance, implies that the number of clusters per volume within the jet is approximately constant.

Acknowledgments

References

Abbas, T., Costen, P., Lockwood, F. C., Romo-Millares, C. A., 1993. The effect of particle size on NO formation in a large-scale pulverized coal-fire laboratory furnace: measurements and modeling. Combustion and Flame 93, 316–326.

Aliseda, A., Cartellier, A., Hainaux, F., Lasheras, J. C., 2002. Effect of preferential concentration on the settling velocity of heavy particles in homogeneous isotropic turbulence. Journal of Fluid Mechanics 468, 77–105.

Annamalai, K., Ryan, W., 1992. Interactive processes in gasification and combustion. part 1: Liquid drop arrays and clouds. Prog. Energy Combust. Sci. 18, 221–295.

Antonia, R. A., Bilger, R. W., 1976. The heated round jet in a coflowing stream. AIAA Journal 14, 1541–1547.

Antonia, R. A., Satyaprakash, B. R., Hussain, A. K. M. F., 1980. Measurements of dissipation rate and some other characteristics of turbulent plane and circular jets. Physics of Fluids 23, 695–700.

Bai, X., Latecki, L. J., Liu, W., 2007. Skeleton pruning by contour partitioning with discrete curve evolution. IEEE transactions on pattern analysis and machine intelligence 29, 449–462.

Bec, J., Biferale, L., Cencini, M., A.Lanotte, Musacchio, S., Toschi, F., 2007. Heavy particle concentration in turbulence at dissipative and inertial scales. Physical Review Letters 98, 084502.

Birzer, C. H., 2012. Correlative analysis of organised structures in turbulent jets. Experiments in Fluids 53, 1681–1691.

Birzer, C. H., Kalt, P. A. M., Nathan, G. J., 2011a. The influences of jet precession on large-scale instantaneous turbulent particle clusters. Int. J. Multiphase Flow 37, 394–402.

Birzer, C. H., Kalt, P. A. M., Nathan, G. J., 2011b. A method to provide statistical measures of large-scale instantaneous particle clusters from planar images. Experiments in Fluids 51, 641–656.

Birzer, C. H., Kalt, P. A. M., Nathan, G. J., 2012. The influences of particle mass loading on mean and instantaneous particle distributions in precessing jet flows. Int. J. Multiphase Flow 41, 12–22.

Blum, H., 1967. A transformation for extracting new descriptors of shape. In: Wathen-Dunn, W. (Ed.), Models for the perception of speech and visual form. pp. 362–380.

Borgefors, G., Nyström, I., Baja, G. S. D., 1999. Computing skeletons in three dimensions. Pattern Recognition 32, 1225–1236.

Calzavarini, E., Kerscher, M., Lohse, D., Toschi, F., 2008. Dimensionality and morphology of particle and bubble clusters in turbulent flow. Journal of Fluid Mechanics 607, 13–24.

Cassel, H. M., Liebman, I., 1959. The cooperative mechanism in the ignition of dust dispersions. Combustion and Flame 3, 467–475.

Chan, Q. N., Medwell, P. R., Nathan, G. J., 2014. Algorithm for soot sheet quantification in a piloted turbulent jet non-premixed natural gas flame. Experiments in Fluids 55, 1827.

Cheng, Y., Torregrosa, M. M., Villegas, A., Diez, F. J., 2011. Time resolved scanning PIV measurements at fine scales in a turbulent jet. International Journal of Heat and Fluid Flow 32, 708–718.

Cheong, M., Birzer, C., Lau, T., 2015. Laser attenuation correction for planar nephelometry concentration measurements. Experimental Techniques, 1–9.

Cho, K. Y., Satija, A., Pourpoint, T. L., Son, S. F., Lucht, R. P., 2014. High-repetition-rate three-dimensional OH imaging using scanned planar laser-induced fluorescence system for multiphase combustion. Applied Optics 53, 316–326.

Eaton, J. K., Fessler, J. R., 1994. Preferential concentration of particles by turbulence. Int. J. Multiphase Flow 20, 169–209.

Eggels, J. G., Unger, F., Weiss, M. H., Westerweel, J., Adrian, R. J., Friedrich, R., Nieuwstadt, F. T., 1994. Fully developed turbulent pipe flow: A comparison between direct numerical simulation and experiment. Journal of Fluid Mechanics 268, 175–209.

Elghobashi, S., 2006. An updated classification map of particle-laden turbulent flows. In: Proceedings of the IUTAM Symposium on Computational Multiphase Flow.

Fessler, J. R., Kulick, J. D., Eaton, J. K., 1994. Preferential concentration of heavy particles in a turbulent channel flow. Physics of Fluids 6, 3742–3749.

Gamba, M., Clemens, N. T., Ezekoye, O. A., 2013. Volumetric PIV and 2D OH PLIF imaging in the far-field of a low Reynolds number nonpremixed jet flame. Meas. Sci. Technol. 24, 1–19.

Goto, S., Vassilicos, J. C., 2006. Self-similar clustering of inertial particles and zero-acceleration points in fully developed two-dimensional turbulence. Physics of Fluids 18, 115103.

Gualtieri, P., Picano, F., Casciola, C. M., 2009. Anisotropic clustering of inertial particles in homogenous shear flow. Journal of Fluid Mechanics 629, 25–39.

Hogan, R. C., Cuzzi, J. N., 2001. Stokes and Reynolds number dependence of preferential particle concentration in simulated three-dimensional turbulence. Physics of Fluids 13, 2938–2945.

Jähne, B., 1997. Practical handbook on image processing for scientific applications. CRC Press.

Kalt, P. A. M., Nathan, G. J., 2007. Corrections to facilitate planar imaging of particle concentration in particle-laden flows using Mie scattering. Part 2: Diverging laser sheets. Applied Optics 46, 7227–7236.

Lau, T. C. W., Nathan, G. J., 2014. The influence of Stokes number on the velocity and concentration distributions in particle-laden jets. Journal of Fluid Mechanics 757, 432–457.

Lau, T. C. W., Nathan, G. J., 2016. The influence of Stokes number on particle clustering at the exit of a turbulent jet issuing from a long round pipe. In: Proceedings of the 9th International Conference on Multiphase Flow. Firenze, Italy.

Longmire, E. K., Eaton, J. K., 1992. Structure of a particle-laden round jet. Journal of Fluid Mechanics 236, 217–257.

Mi, J., Nobes, D. S., Nathan, G. J., 2001. Influence of jet exit conditions on the passive scalar field of an axisymmetric free jet. Journal of Fluid Mechanics 432, 91–125.

Monchaux, R., Bourgoin, M., Cartellier, A., 2010. Preferential concentration of heavy particles: A Voronoï analysis. Physics of Fluids 22, 103304.

Monchaux, R., Bourgoin, M., Cartellier, A., 2012. Analyzing preferential concentration and clustering of inertial particles in turbulence. International Journal of Multiphase Flow 40, 1–18.

Obligado, M., Teitelbaum, T., Cartellier, A., Mininni, P., Bourgoin, M., 2014. Preferential concentration of heavy particles in turbulence. Journal of Turbulence 15, 293–310.

Qamar, N. H., Nathan, G. J., Alwahabi, Z. T., Chan, Q. N., 2011. Soot sheet dimensions in turbulent nonpremixed flames. Combustion and Flame 158, 2458–2464.

Rouson, D. W. I., Eaton, J. K., 2001. On the preferential concentration of solid particles in turbulent channel flow. Journal of Fluid Mechanics 428, 149–169.

Russ, J. C., 2002. The image processing handbook. CRC Press, Berlin Heidelberg.

Salazar, J. P. L. C., Jong, J. D., Cao, L., Woodward, S. H., Meng, H., Collins, L. R., 2008. Experimental and numerical investigation of inertial particle clustering in isotropic turbulence. Journal of Fluid Mechanics 600, 245–256.

Saw, E. W., Shaw, R. A., Ayyalasomayajula, S., Chuang, P. Y., Gylfason, A., 2008. Inertial clustering of particles in high-Reynolds-number turbulence. Physical Review Letters 100, 214501.

Shaked, D., Bruckstein, A. M., 1998. Pruning medial axis. Computer vision and image understanding 69, 156–169.

Smith, N. L., Nathan, G. J., Zhang, D. K., Nobes, D. S., 2002. The significance of particle clustering in pulverized coal flames. Proceedings of the Combustion Institute 29, 797–804.

Soille, P., 1999. Morphological image analysis. Springer.

Thurow, B. S., Lynch, K. P., 2009. Development of a high-speed three-dimensional flow visualization technique. AIAA Journal 47, 2857–2865.

Villermaux, E., Duplat, J., 2006. Coarse grained scale of turbulent mixtures. Physical Review Letters 97 (144506).

Wang, L., Maxey, M. R., 1993. Settling velocity and concentration distribution of heavy particles in homogeneous isotropic turbulence. Journal of Fluid Mechanics 256, 27–68.

Wellander, R., Richter, M., Aldén, M., 2011. Time resolved, 3D imaging 4D of two phase flow at a repetition rate of 1 kHz. Optics Express 19, 21508–21514.

Yoshimoto, H., Goto, S., 2007. Self-similar clustering of inertial particles in homogeneous turbulence. Journal of Fluid Mechanics 577, 275–286.

Zimmer, L., Ikeda, Y., 2003. Planar droplet sizing for the characterization of droplet clusters in an industrial gun-type burner. Part. Part. Syst. Charact. 20, 199–208.

19